Aalto University

Adam, R.; Ade, P. A R; Aghanim, N.; Ashdown, M.; Aumont, J.; Baccigalupi, C.; Banday, A. J.; Barreiro, R. B.; Bartolo, N.; Battaner, E.; Benabed, K.; Benoit-Lévy, A.; Bersanelli, M.; Bielewicz, P.; Bikmaev, I.; Bonaldi, A.; Bond, J. R.; Borrill, J.; Bouchet, F. R.; Burenin, R.; Burigana, C.; Calabrese, E.; Cardoso, J. F.; Catalano, A.; Chiang, H. C.; Christensen, P. R.; Churazov, E.; Colombo, L. P L; Combet, C.; Comis, B.; Couchot, F.; Crill, B. P.; Curto, A.; Cuttaia, F.; Danese, L.; Davis, R. J.; De Bernardis, P.; De Rosa, A.; De Zotti, G.; Delabrouille, J.; Désert, F. X.; Diego, J. M.; Dole, H.; Doré, O.; Douspis, M.; Ducout, A.; Dupac, X.; Elsner, F.; Enßlin, T. A.; Finelli, F.

Planck intermediate results

Planck intermediate results

XLIII. Spectral energy distribution of dust in clusters of galaxies

Planck Collaboration: R. Adam[73], P. A. R. Ade[87], N. Aghanim[58], M. Ashdown[67,7], J. Aumont[58], C. Baccigalupi[85], A. J. Banday[96,12],
R. B. Barreiro[63], N. Bartolo[30,64], E. Battaner[97,98], K. Benabed[59,95], A. Benoit-Lévy[26,59,95], M. Bersanelli[33,48], P. Bielewicz[80,12,85], I. Bikmaev[22,3],
A. Bonaldi[66], J. R. Bond[11], J. Borrill[15,90], F. R. Bouchet[59,88], R. Burenin[89,78], C. Burigana[47,31,49], E. Calabrese[92], J.-F. Cardoso[72,1,59],
A. Catalano[73,70], H. C. Chiang[28,8], P. R. Christensen[81,36], E. Churazov[77,89], L. P. L. Colombo[25,65], C. Combet[73], B. Comis[73,*], F. Couchot[69],
B. P. Crill[65,13], A. Curto[63,7,67], F. Cuttaia[47], L. Danese[85], R. J. Davis[66], P. de Bernardis[32], A. de Rosa[47], G. de Zotti[44,85], J. Delabrouille[1],
F.-X. Désert[54], J. M. Diego[63], H. Dole[58,57], M. Douspis[58], A. Ducout[59,55], X. Dupac[39], F. Elsner[26,59,95], T. A. Enßlin[77], F. Finelli[47,49],
O. Forni[96,12], M. Frailis[46], A. A. Fraisse[28], E. Franceschi[47], S. Galeotta[46], K. Ganga[1], R. T. Génova-Santos[62,20], M. Giard[96,12], Y. Giraud-Héraud[1],
E. Gjerløw[61], J. González-Nuevo[21,63], K. M. Górski[65,99], A. Gregorio[34,46,53], A. Gruppuso[47], J. E. Gudmundsson[94,83,28], F. K. Hansen[61],
D. L. Harrison[60,67], C. Hernández-Monteagudo[14,77], D. Herranz[63], S. R. Hildebrandt[65,13], E. Hivon[59,95], M. Hobson[7], A. Hornstrup[18],
W. Hovest[77], G. Hurier[58], A. H. Jaffe[55], T. R. Jaffe[96,12], W. C. Jones[28], E. Keihänen[27], R. Keskitalo[15], I. Khamitov[93,22], T. S. Kisner[75],
R. Kneissl[38,9], J. Knoche[77], M. Kunz[19,58,4], H. Kurki-Suonio[27,43], G. Lagache[6,58], A. Lähteenmäki[2,43], J.-M. Lamarre[70], A. Lasenby[7,67],
M. Lattanzi[31,50], C. R. Lawrence[65], R. Leonardi[10], F. Levrier[70], M. Liguori[30,64], P. B. Lilje[61], M. Linden-Vørnle[18], M. López-Caniego[39,63],
J. F. Macías-Pérez[73], B. Maffei[66], G. Maggio[46], N. Mandolesi[47,31], A. Mangilli[58,69], M. Maris[46], P. G. Martin[11], E. Martínez-González[63],
S. Masi[32], S. Matarrese[30,64,41], A. Melchiorri[32,51], A. Mennella[33,48], M. Migliaccio[60,67], M.-A. Miville-Deschênes[58,11], A. Moneti[59],
L. Montier[96,12], G. Morgante[47], D. Mortlock[55], D. Munshi[87], J. A. Murphy[79], P. Naselsky[82,37], F. Nati[28], P. Natoli[31,5,50],
H. U. Nørgaard-Nielsen[18], D. Novikov[76], I. Novikov[81,76], C. A. Oxborrow[18], L. Pagano[32,51], F. Pajot[58], D. Paoletti[47,49], F. Pasian[46],
O. Perdereau[69], L. Perotto[73], V. Pettorino[42], F. Piacentini[32], M. Piat[1], S. Plaszczynski[69], E. Pointecouteau[96,12], G. Polenta[5,45], N. Ponthieu[58,54],
G. W. Pratt[71], S. Prunet[59,95], J.-L. Puget[58], J. P. Rachen[23,77], R. Rebolo[62,16,20], M. Reinecke[77], M. Remazeilles[66,58,1], C. Renault[73], A. Renzi[35,52],
I. Ristorcelli[96,12], G. Rocha[65,13], C. Rosset[1], M. Rossetti[33,48], G. Roudier[1,70,65], J. A. Rubiño-Martín[62,20], B. Rusholme[56], D. Santos[73],
M. Savelainen[27,43], G. Savini[84], D. Scott[24], V. Stolyarov[7,91,68], R. Stompor[1], R. Sudiwala[87], R. Sunyaev[77,89], D. Sutton[60,67], A.-S. Suur-Uski[27,43],
J.-F. Sygnet[59], J. A. Tauber[40], L. Terenzi[86,47], L. Toffolatti[21,63,47], M. Tomasi[33,48], M. Tristram[69], M. Tucci[19], L. Valenziano[47], J. Valiviita[27,43],
F. Van Tent[74], P. Vielva[63], F. Villa[47], L. A. Wade[65], I. K. Wehus[65,61], D. Yvon[17], A. Zacchei[46], and A. Zonca[29]

(Affiliations can be found after the references)

ABSTRACT

Although infrared (IR) overall dust emission from clusters of galaxies has been statistically detected using data from the Infrared Astronomical Satellite (IRAS), it has not been possible to sample the spectral energy distribution (SED) of this emission over its peak, and thus to break the degeneracy between dust temperature and mass. By complementing the IRAS spectral coverage with *Planck* satellite data from 100 to 857 GHz, we provide new constraints on the IR spectrum of thermal dust emission in clusters of galaxies. We achieve this by using a stacking approach for a sample of several hundred objects from the *Planck* cluster sample. This procedure averages out fluctuations from the IR sky, allowing us to reach a significant detection of the faint cluster contribution. We also use the large frequency range probed by *Planck*, together with component-separation techniques, to remove the contamination from both cosmic microwave background anisotropies and the thermal Sunyaev-Zeldovich effect (tSZ) signal, which dominate at $\nu \leq 353$ GHz. By excluding dominant spurious signals or systematic effects, averaged detections are reported at frequencies 353 GHz $\leq \nu \leq 5000$ GHz. We confirm the presence of dust in clusters of galaxies at low and intermediate redshifts, yielding an SED with a shape similar to that of the Milky Way. *Planck*'s resolution does not allow us to investigate the detailed spatial distribution of this emission (e.g. whether it comes from intergalactic dust or simply the dust content of the cluster galaxies), but the radial distribution of the emission appears to follow that of the stacked SZ signal, and thus the extent of the clusters. The recovered SED allows us to constrain the dust mass responsible for the signal and its temperature.

Key words. galaxies: clusters: intracluster medium – galaxies: clusters: general – diffuse radiation – infrared: general

1. Introduction

In clusters of galaxies, the bulk of the baryonic mass is a hot (roughly 10^7–10^8 K), ionized, diffuse gas, mostly emitting at X-ray wavelengths (e.g. Sarazin 1986). However, since the very beginning, X-ray spectroscopy has shown the presence of heavy elements within the intracluster medium (ICM), presumably owing to stripping of interstellar matter from galaxies, dusty winds from intracluster stars, and AGN interaction with the ICM (e.g. Sarazin 1988). But the ICM is a hostile environment for dust grains. The strong thermal sputtering that dust grains undergo

at cluster cores implies lifetimes ranging from 10^6 to 10^9 yr (Dwek & Arendt 1992), depending on the gas density and grain size. Thus, with only the most recently injected material surviving, the cluster dust content is significantly lower than the typical interstellar values. Nevertheless, despite these lower values, dust can have a non-negligible role in the cooling/heating of the intracluster gas (Dwek et al. 1990; Popescu et al. 2000; Montier & Giard 2004; Weingartner et al. 2006) and in influencing the formation and evolution of clusters and their overall properties (i.e. cluster scaling relations, da Silva et al. 2009).

In order to study the effects of cluster environment on the evolution of the member galaxies, several studies have been conducted on the dust component of galaxies that are in clusters (e.g.

Braglia et al. 2011 with BLAST data, Coppin et al. 2011 with *Herschel* data) and in massive dark matter halos (Welikala et al. 2016, approximately $10^{13} M_\odot$ at $z \sim 1$). However, less has been done on extended dust emission in clusters. Heated by collisions with the hot X-ray emitting cluster gas, ICM dust grains are in fact expected to emit at far-infrared (FIR) wavelengths (Dwek et al. 1990) and contribute to the diffuse infrared (IR) emission from clusters. Stickel et al. (2002) used the Infrared Space Observatory (ISO) to look for the extended FIR emission in six Abell clusters; only towards one of them (A1656, the Coma cluster) did they find a localized excess of the ratio between the signal at $120\,\mu$m and $180\,\mu$m, interpreted as being due to thermal emission from intracluster dust distributed in the ICM, with an approximate mass estimate of $10^7 M_\odot$. Additionally, although in qualitative agreement with the ISO result, Kitayama et al. (2009) found only marginal evidence for this central excess in Coma, based on *Spitzer* data. On the other hand, using a different approach and correlating the Sloan Digital Sky Survey catalogues of clusters and quasars (behind clusters and in the field), Chelouche et al. (2007) measured a reddening, typical of dust, towards galaxy clusters at $z \simeq 0.2$, showing that most of the detected dust lies in the outskirts of the clusters.

A direct study of the IR-emitting dust in clusters is difficult because the fluctuations of the IR sky are of larger amplitude than the flux expected from a single cluster. However, by averaging many small patches centred on known cluster positions, a stacking approach can be used to increase the signal-to-noise ratio, while averaging down the fluctuations of the IR sky. This statistical approach was applied for the first time by Kelly & Rieke (1990) considering 71 clusters of galaxies and IRAS data. A similar method was also the basis of the detection of the cluster IR signal reported by Montier & Giard (2005), who exploited the four-band observations provided by IRAS for a sample of 11 507 objects. Later, Giard et al. (2008) explored the redshift evolution of the IR luminosity of clusters compared with the X-ray luminosities of the clusters. More recently, this approach was used in Planck Collaboration XXIII (2016), where the correlation between the SZ effect and the IR emission was studied for a specific sample of clusters.

When dealing with arcminute resolution data, like those of *Planck*[1] and IRAS, the main difficulty for the characterization of the IR properties of clusters of galaxies is to disentangle the contributions to the overall IR luminosity coming from the cluster galaxies and that coming from the ICM. The overall IR flux is expected to be dominated by the dust emission of the galaxy component, in particular from star-forming galaxies. Roncarelli et al. (2010) reconstructed the IRAS stacked flux derived by Montier & Giard (2005) by modelling the galaxy population (using the SDSS-maxBCG catalogue, consisting of approximately 11 500 objects with $0.1 < z < 0.3$), leaving little room for the contribution of intra-cluster dust. However, both the amount of mass in the form of dust and its location in the clusters, are still open issues. If the dust temperature is only poorly constrained, we can obtain only limited constraints on the corresponding dust mass. In this work, following the method adopted in Montier & Giard (2005) and Giard et al. (2008), we combine IRAS and *Planck* data, stack these at the positions of the *Planck* cluster sample (Planck Collaboration XXIX 2014)

and investigate the extension and nature of the corresponding IR signal. Thanks to the complementary spectral coverage of the two satellites, we are able to sample the IR emission over its peak in frequency. With a maximum wavelength of $100\,\mu$m, IRAS can only explore the warm dust component, while it is the cold dust that represents the bulk of the overall dust mass.

The paper is organized as follows. Section 2 presents the data used for this study. We then detail in Sect. 3 the stacking approach, before discussing the results in Sect. 4. We summarize and conclude in Sect. 5.

2. Data sets

2.1. Planck data

2.1.1. Frequency maps

The *Planck* High Frequency Instrument (HFI) enables us to explore the complementary side of the IR spectrum $(100-857\,$GHz), compared with previous studies based on IRAS data $(100-12\,\mu$m). This paper is based on the full (29 month) *Planck*-HFI mission, corresponding to about five complete sky surveys (Planck Collaboration I 2016). We use maps from the six HFI frequency channels (convolved to a common resolution of 10′), pixelized using the `HEALPix` scheme (Górski et al. 2005) at $N_{\rm side} = 2048$ at full resolution.

2.1.2. Contamination maps

While we expect dust emission to be the strongest signal at both 545 and 857 GHz, at $\nu \leq 217$ GHz the intensity maps will be dominated by cosmic microwave background (CMB) temperature anisotropies. Furthermore, since we want to examine known cluster positions on the sky, we must also deal with the signal from the thermal Sunyaev-Zeldovich (tSZ) effect (Sunyaev & Zeldovich 1972, 1980). This latter signal is produced by the inverse Compton interaction of CMB photons with the hot electrons of the ICM. The tSZ contribution will be the dominant signal at 100 GHz and 143 GHz (where it shows up as a lower CMB temperature), negligible at 217 GHz (since this is close to the SZ null), and also significant at 353 GHz (where it shows up as a higher CMB temperature). Separating the tSZ contribution from thermal dust emission at $\nu \leq 353$ GHz is a difficult task, which can only be achieved if the spectrum of the sources is sufficiently well sampled in the frequency domain. This is the case for the *Planck* satellite, whose wide frequency range allows us to reconstruct full-sky maps of both the CMB and tSZ effect (y-map, Planck Collaboration XXI 2014; Planck Collaboration XXII 2016) using adapted component-separation techniques.

These maps have been produced using `MILCA` (the Modified Internal Linear Combination Algorithm, Hurier et al. 2013) with 10′ resolution. The method is based on the well known internal linear combination (ILC) approach that searches for the linear combination of the input maps, which minimizes the variance of the final reconstructed signal, under the constraint of offering unit gain to the component of interest, whose spectral behaviour is known. The quality of the MILCA y-map reconstruction has been tested in several ways in the past, comparing different flux reconstruction methods, on data and simulations (e.g. Planck Collaboration Int. V 2013; Hurier et al. 2013; Planck Collaboration XXII 2016).

---

[1] *Planck* (http://www.esa.int/Planck) is a project of the European Space Agency (ESA) with instruments provided by two scientific consortia funded by ESA member states and led by Principal Investigators from France and Italy, telescope reflectors provided through a collaboration between ESA and a scientific consortium led and funded by Denmark, and additional contributions from NASA (USA).

The reconstructed maps have been used to remove the tSZ signal and the CMB anisotropies, which dominate the stacked maps at frequencies lower than 353 GHz. The tSZ map also has the advantage of probing the extension of the clusters, providing a means to check that the IR signal belongs to the cluster.

Compared to the publicly released CMB map (specifically SMICA, available through the *Planck* Legacy Archive[2]), the reconstruction obtained with MILCA, imposing conditions to preserve the CMB and remove the SZ effect, allows us to obtain a more robust extraction of the CMB signal at each cluster position. The SMICA CMB map is, however, more reliable at large angular scales and has been used to test the robustness of the CMB reconstruction at scales of 1°. The SMICA map has allowed us to validate the MILCA map in the region around each cluster position (0.°5).

2.1.3. Cluster sample: the *Planck* Catalogue of SZ Sources

In order to stack at known cluster positions in rather clean sky regions (e.g. with low Galactic dust contamination), we consider the clusters listed in the *Planck* Catalogue of SZ sources (Planck Collaboration XXIX 2014). For such high significance SZ-detected clusters ($S/N > 4.5$) belonging to *Planck* SZ catalogues, the robustness of the tSZ flux reconstruction has been already investigated and tested (Planck Collaboration XXI 2014; Planck Collaboration XXII 2016). We expect to be able to subtract the tSZ signal with high accuracy ($\ll 10\%$), which is necessary in order to reconstruct the spectral energy distribution (SED) of the IR emission from clusters at $\nu \leq 353$ GHz.

The SZ catalogue constructed from the total intensity data taken during the first 15.5 months of *Planck* observations (Planck Collaboration XXIX 2014, PSZ1 hereafter) contains 1227 clusters and cluster candidates. We limit our analysis to PSZ1 since, unlike for the Second Catalogue of *Planck* SZ sources (Planck Collaboration XXVII 2016, PSZ2), its validation process and extensive follow-up observations have already been completed (as detailed in Planck Collaboration Int. XXXVI 2016; Planck Collaboration Int. XXVI 2015; Planck Collaboration XXXII 2015), providing redshifts and associated mass estimates (derived from the Y_z mass proxy, as detailed in Sect. 7.2.2 of Planck Collaboration XXIX 2014) for 913 objects out to 1227. As it will be discussed later (Sect. 3.1), to maximize the size of the sample, the selection of the fields to be stacked has been done starting from the list of 1227 objects, with no preference for those with redshift information.

2.2. IRAS data

To sample the thermal dust SED across its peak and to constrain its shape, we complement the *Planck* spectral coverage with the 100 and 60-μm IRAS maps. We explicitly use the Improved Reprocessing of the IRAS Survey maps (IRIS[3], Miville-Deschênes & Lagache 2005), for which artefacts such as zero level, calibration, striping, and residual zodiacal light have been corrected. Here, we have used the corresponding sky maps provided in HEALPix format (Gorski et al. 1999), with $N_{side} = 2048$. For the purposes of the present work, the IRIS 100 and 60 μm maps are convolved to a resolution of 10′ in order to match that of the *Planck* frequency and tSZ maps.

---

3. Stacking analysis

Because the sky fluctuations from the cosmic infrared background (CIB) are stronger than the brightness expected from a single object, we cannot detect the dust contribution to the IR emission from individual clusters of galaxies. However, we can statistically detect the population of clusters by averaging local maps centred at known cluster positions, thereby reducing the background fluctuations (see e.g. Montier & Giard 2005; Giard et al. 2008). Here we take advantage of the "IAS stacking library" (Bavouzet et al. 2008; Béthermin et al. 2010) in order to co-add cluster-centred regions and increase the statistical significance of the IR signal at each frequency. Patches of $2° \times 2°$, centred on the cluster positions (using 2′ pixels) have been extracted for the six *Planck*-HFI frequency channels, as well as for the 100 and 60-μm IRIS maps. To ensure a high signal-to-noise ratio and low level of contamination, the low reliability ("category 3") PSZ1 cluster candidates (126 objects out of 1227) have been excluded from the analysis.

We now detail the different steps of the stacking approach that we adopt to perform our analysis. This includes extraction of the maps at each frequency, foreground removal, and selection of the final cluster sample.

3.1. Field selection

3.1.1. Exclusion of CO contaminated regions

The 100, 217, and 353-GHz *Planck* channels can be significantly contaminated by the signal due to the emission of CO rotational transition lines at 115, 230, and 345 GHz, respectively (Planck Collaboration IX 2014). Component separation methods have been used to reconstruct CO maps from *Planck* data (Planck Collaboration et al. 2014). Since the CO emission can be an important foreground for the purpose of the present work, we choose to use a quite strict CO mask. This mask is based on the released CO $J = 1 \rightarrow 0$ *Planck* map (Planck Collaboration et al. 2014) and it has been obtained by applying a $3 K_{RJ}$ km s^{-1} cut on the CO map (where the K_{RJ} unit comes from intensity scaled to temperature using the Rayleigh-Jeans approximation). We conservatively exclude from the stacking procedure all the fields in which we find flagged pixels, according to the CO mask, at cluster-centric distances ≤1°. This leads to the exclusion of 55 extra clusters, living us with 1046 remaining clusters.

3.1.2. Point source mask

Before proceeding to stack the cluster-centred fields, we check that they are characterized by comparable background contributions. As a first step we verify the presence of known point sources, using the masks provided by the Planck Collaboration for the six frequencies considered here, as well as the IRAS point source catalogue (Helou & Walker 1988). We exclude all fields in which point sources are found at cluster-centric distances ≤5′, even if this is the case only for a single channel. For point sources at larger distances from the nominal cluster position we set the corresponding pixel values to the mean for the pixels within the $0.°5 \leq r < 1°$ region of the $2° \times 2°$ patch, at each wavelength. We also check that all the selected cluster fields have a variance in the $0.°5 \leq r < 1°$ region that is ≤5 times that of the whole sample. These additional cuts lead to a reduced sample of 645 clusters, with only two clusters lying at Galactic latitudes lower than 10°. We have also tested the more conservative choice of excluding
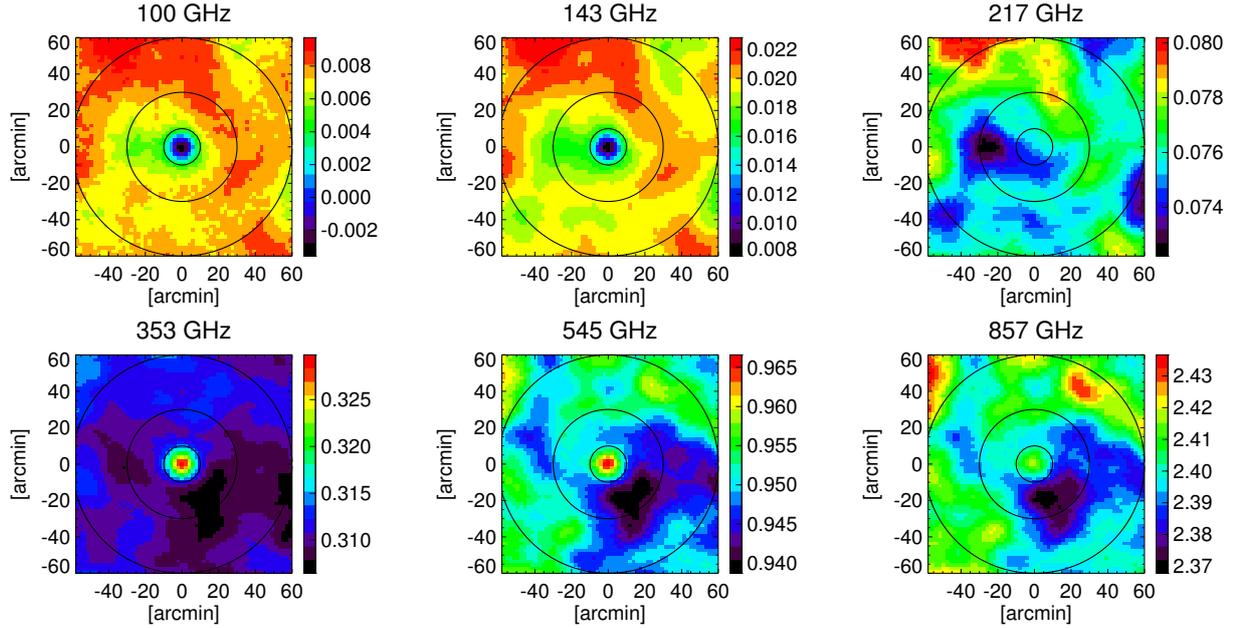
Fig. 1. *Planck* stacked maps at the positions of the final sample of 645 clusters. The maps are $2° \times 2°$ in size and are in units of MJy sr^{-1}. Black contours represent circles with a radius equal to $10'$, $30'$, and $60'$.

all the fields in which known point sources are found at $\leq 10'$ from the centre. This substantially reduces the sample size (to 504 clusters), while giving no significant difference in the recovered signal, as will be discussed later.

3.2. Stacking of the selected fields

We give the same weight to all the cluster fields, since having a particular cluster dominate the average signal is not useful for the purposes of examining the properties of the whole population. The choice of using a constant patch size is motivated by the fact that the differences in cluster angular sizes are negligible when dealing with a $10'$ resolution map. Even if a few tens of very low-z clusters (say $z < 0.1$) are present within the final sample, the average typical size of the sample clusters ($\theta_{500} = 7'.4 \pm 5'.3$, with a median of $5'.7$) allows us to integrate the total flux in the stacked maps within a fixed radius, which we choose to be $15'$. The suitability of this choice is verified by looking at the integrated signal as a function of aperture radius.

In Fig. 1 we show the stacked $2° \times 2°$ patches, for the *Planck*-HFI frequencies. Since no foreground or offset removal has been performed the dust signature is not easily apparent, but instead we can see the negative tSZ signal dominating at $\nu \leq 143$ GHz and CMB anisotropies at 217 GHz, with the dust contribution becoming stronger at $\nu \geq 353$ GHz. We also stack the CMB and tSZ maps (Sect. 2.1.2), i.e. $\Sigma_i M^i_{CMB}$ and $\Sigma_i M^i_{tSZ}$, summing over all the selected clusters i. These two quantities are then subtracted from the raw frequency maps ($\Sigma_i M^i_\nu$ shown in Fig. 1), specifically calculating $M'_\nu = (\Sigma_i M^i_\nu - \Sigma_i M^i_{CMB} - \Sigma_i f_{tSZ,\nu} M^i_{SZ})/N$, where $f_{tSZ,\nu}$ is the conversion factor from the tSZ Compton parameter y to MJy sr^{-1} for each frequency ν. Following Giard et al. (2008), we then perform a background-subtraction procedure by fitting a 3rd-order polynomial surface to the map region for which the cluster-centric distance is above $10'$. Finally we also subtract the average signal found for pixels with a distance from the centre that lies between $0°.5$ and $1°$, which is used to compute the zero level of the map.

The cleaned and stacked maps are shown in Fig. 2. The same results are obtained if foregrounds and offsets are subtracted cluster by cluster or if we directly stack the cleaned cluster-centred patches. Although we already have hints of a signal at the centre of 143 GHz map, the detection of a significant central positive peak starts at 217 GHz, and is very clearly observed at $\nu \geq 353$ GHz. Between 100 and 217 GHz the signal is expected to be fainter, according to the typical SED of thermal dust emission. The black contours in Fig. 2 allow comparison with the distribution of the cluster hot gas, representing where the stacked y-map has a value that is 0.5, 0.1, and 0 times its maximum. As expected, the recovered IR emission follows the distribution of the main cluster baryonic component, and thus the extent of the clusters. The average intensity profiles as a function of radius are also provided in Fig. A.1.

Since IR dust emission cannot be detected for individual clusters, average values have been obtained, and the associated uncertainties determined using a bootstrap approach. This consists of constructing and stacking many (300) cluster samples obtained by randomly replacing sources from the original sample, so that each of them contains the same number of clusters as the initial one. The statistical properties of the population being stacked can be then determined by looking at the mean and standard deviation of the flux found in the stacked maps corresponding to each of the resampled cluster lists. We checked that the average values obtained with this resampling technique are equal to what we obtained directly on the original stacked map (without any resampling). This is important, since it indicates that we are indeed stacking a homogeneous population of objects, and that the detected signal is not due to only a small number of a clusters. The mean values recovered are also consistent with the expectations described in Montier & Giard (2005), given the redshift distribution of the sample considered here.

In Table 1 we report, for each frequency: the average fluxes, F, found when integrating out to $15'$ from the centre; the standard deviation found using the bootstrap resampling, ΔF_b; and an estimate of the uncertainty on the flux at each frequency, ΔF. The flux uncertainties, ΔF, have been obtained as the standard
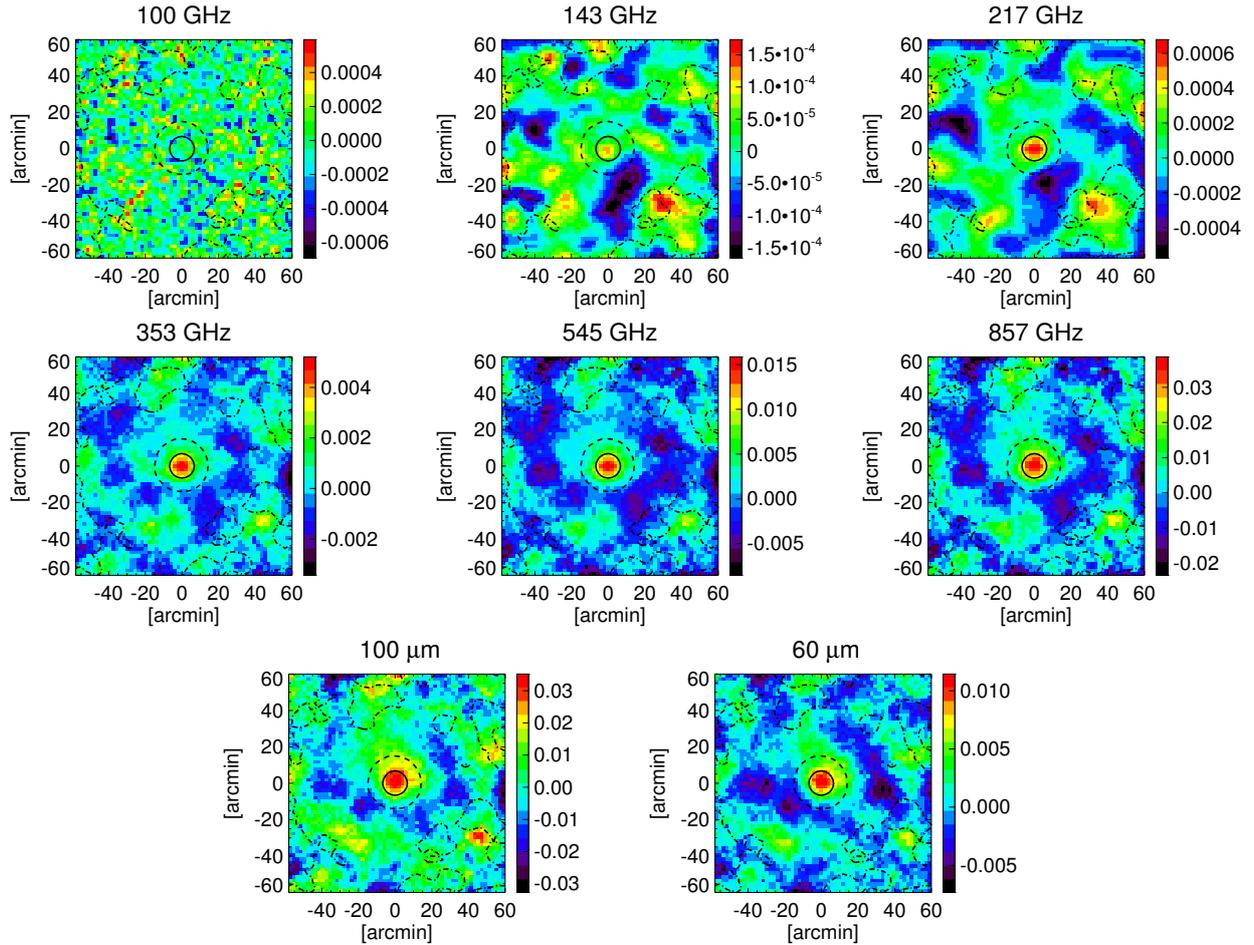
Fig. 2. Background- and foreground-cleaned stacked maps, for the final sample of 645 clusters. The units here are MJy sr^{-1}. The extent of the stacked y-signal is represented by black contours for regions of 0.5, 0.1, and 0 times the maximum of the signal (in solid, dashed, and dot-dashed lines, respectively). See Sect. 3.2 for further details.

deviation of the fluxes found at random positions in a $2° \times 2°$ region, located further than $15'$ from the centre, both using the cluster-centred stacked maps and the "depointed" stacked maps (discussed in Sect. 3.3).

3.3. Robustness tests

In order to test the robustness of our results, we have performed various checks, following an approach similar to that of Montier & Giard (2005). Figure 3 shows the $2° \times 2°$ depointed maps that we obtain at 857 GHz when we repeat the same stacking procedure by changing the cluster Galactic longitudes and/or latitudes by $\pm1°$. This has been done for all the frequency channels and shows that the detection is not an artefact of the adopted stacking scheme. The mean of the fluxes obtained at the centre of the depointed regions is consistent with zero within the uncertainties (i.e. ΔF).

The approach adopted to derive the uncertainty on the flux ΔF has also been applied to a random sample of positions on the sky, whose Galactic latitude distribution follows that of the real clusters in our sample. The derived uncertainties, ΔF_{ran}, are listed in Table 1. As for the depointed regions, the mean fluxes obtained at the centre of the random patches are consistent with zero, within the given uncertainties. The values obtained for ΔF_{ran} are systematically higher than ΔF. This was to be expected, since *Planck* blind tSZ detections are more likely in
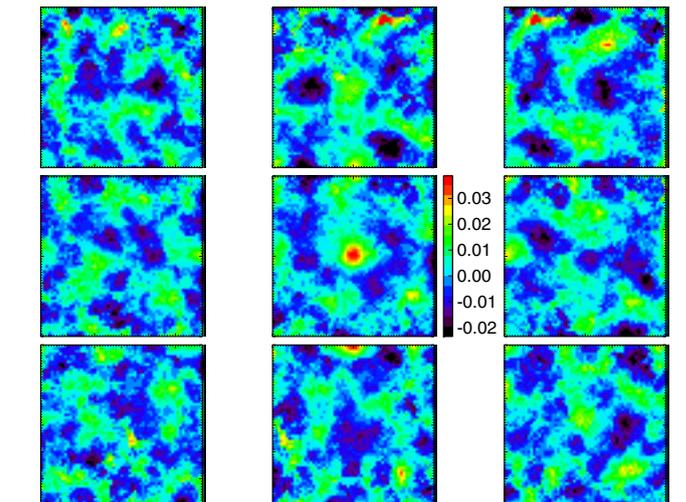
Fig. 3. Tests of stacking on "depointed" regions. The *central panel* shows the stacked result obtained at 857 GHz for the 645 cluster-centred patches (as in Fig. 2). This is surrounded by the eight neighboring maps obtained by changing the cluster Galactic longitude or latitude (or both) by $\pm1°$.

regions that are cleaner of dust contamination. For different cuts in Galactic latitude, moving away from the Galactic plane, ΔF_{ran}

Table 1. Fluxes found in the co-added maps for a sample of 645 clusters extracted from the first *Planck* Catalogue of SZ sources.

	F [Jy]	$\Delta F_{\rm b}$ [Jy]	ΔF [Jy]	$\Delta F_{\rm ran}$ [Jy]
100 GHz	-0.0009	± 0.0031	± 0.0028	± 0.0031
143 GHz	0.0010	± 0.0030	± 0.0023	± 0.0034
217 GHz	0.0103	± 0.0092	± 0.0056	± 0.012
353 GHz	0.098	± 0.036	± 0.020	± 0.042
545 GHz	0.34	± 0.12	± 0.063	± 0.13
853 GHz	0.94	± 0.33	± 0.18	± 0.34
$100\,\mu$m	0.86	± 0.40	± 0.22	± 0.59
$60\,\mu$m	0.269	± 0.097	± 0.083	± 0.34

Notes. $\Delta F_{\rm b}$ is the uncertainty estimated using bootstrap resampling, while ΔF is obtained by integrating at random positions around the cluster and around the regions centred 1° away from the cluster Galactic latitude and longitude (see Sect. 3.3 and Fig. 3), and $\Delta F_{\rm ran}$ is determined the same way as $\Delta F_{\rm d}$ except replacing the cluster position with random positions on the sky.

decreases. This might indicate that some residual contamination due to Galactic dust emission is present. Indeed, in Fig. 2 we can see a correlation between frequencies for the residual fluctuations in the region surrounding the clusters. Such a correlation between frequencies could be also introduced by the process of subtracting the contamination maps (CMB and tSZ), since these are built from the same *Planck*-HFI maps. However the CMB anisotropies and the tSZ signal are both negligible at $\nu \geq 545$ GHz. The uncertainty $\Delta F_{\rm ran}$ is of the order of $\Delta F_{\rm b}$ and ΔF at the frequencies for which we have a significant detection; hence this contribution does not dominate the signal and we can consider it to be accounted for in the error budget. For this reason, we do not impose any extra selection cut in Galactic latitude in order to maximize the sample size.

As a further cross-check, we have tested the robustness of the results by alternatively adding and subtracting the patches centred at the cluster positions. This approach shows that none of the individual patches dominates the final average signal, in agreement with the results of the bootstrap resampling procedure.

4. SED of the cluster IR emission

4.1. SED model

Using the cleaned stacked maps obtained in Sect. 3, we derive the IR fluxes for each of the frequencies considered. In Fig. 4 we show the average SED of galaxy clusters from $60\,\mu$m to 3 mm (as listed in Table 1).

The SED shown in Fig. 4 behaves like Galactic dust, confirming the hypothesis of thermal dust emission. It can be well represented by modified blackbody emission (the black curve in Fig. 4), with spectral index β. This accounts for the fact that the IR emission from clusters is not a perfect blackbody, but has a power-law dust emissivity $\kappa_\nu = \kappa_0 (\nu/\nu_0)^\beta$, i.e.

$$I_\nu = A_0 \left(\frac{\nu}{\nu_0}\right)^\beta B_\nu(T_{\rm d0}), \qquad (1)$$

where β is the emissivity index, B_ν is the Planck function, $T_{\rm d0}$ the dust temperature, and A_0 an overall amplitude. The combination of *Planck* and IRAS spectral coverage allows us to sample the SED of the average IR cluster across its emission peak. The reconstructed SED can be used to constrain the dust temperature
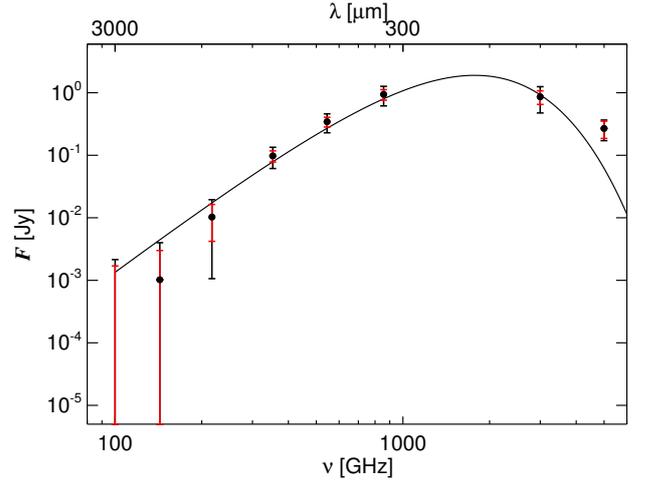
Fig. 4. Average SED for galaxy clusters. In black points we show the flux, as a function of frequency, found in the co-added maps obtained for a sample of 645 clusters. The error bars in black correspond to the dispersion estimated using bootstrap resampling ($\Delta F_{\rm b}$, Table 1). The red error bars have been estimated as the standard deviation of the flux integrated at random positions away from each cluster region (ΔF, Table 1). The black solid line shows the best-fit modified blackbody model (with $\beta = 1.5$). We note that the highest frequency point ($60\,\mu$m from IRAS) is not used in the fit.

and also the amplitude A_0, which is directly related to the dust mass. Following the prescription of Hildebrand (1983), the dust mass can be in fact estimated from the observed flux densities and the modified blackbody temperature as

$$M_{\rm d} = \frac{S_\nu D^2 (1+z) K}{\kappa_\nu B_\nu(T_{\rm d0})}, \qquad (2)$$

with the "K-correction" being

$$K = \left(\frac{\nu_{\rm obs}}{\nu_{\rm em}}\right)^{3+\beta} \frac{{\rm e}^{(h\nu_{\rm em}/kT_{\rm d0})} - 1}{{\rm e}^{(\nu_{\rm obs}/kT_{\rm d0})} - 1}, \qquad (3)$$

which allows translation to monochromatic rest-frame flux densities, S_ν. Here $\nu_{\rm obs}$ represents the observed frequency and $\nu_{\rm em}$ the rest-frame frequency, with $\nu_{\rm obs} = \nu_{\rm em}/(1+z)$, and D is the radial comoving distance. The amplitude parameter A_0 then provides an estimate of the overall dust mass:

$$M_{\rm d} = \frac{A_0}{\kappa_{\nu_0}} \Omega D^2 (1+z) K, \qquad (4)$$

provided we know κ_{ν_0}, the dust opacity at a given frequency ν_0, with Ω being the solid angle. Here we adopt the value $\kappa_{850} = 0.0383$ m^2 kg^{-1} (Draine 2003).

This model has the advantage of being accurate enough to adequately fit the data, while providing a simple interpretation of the observations, with a small number of parameters. Even though studies of star-forming galaxies have demonstrated the inadequacy of a single temperature model for detailed, high signal-to-noise SED shapes (e.g. Dale & Helou 2002; Wiklind 2003), the cold dust component ($\lambda \gtrsim 100\,\mu$m) tends to be well represented using a single effective temperature modified blackbody (Draine & Li 2007; Casey 2012; Clemens et al. 2013). Figure 4 shows that a further component would indeed permit us to also fit the $60\,\mu$m point (the rightmost point in Fig. 4). This excess at high frequency could be caused by smaller grains that are not in thermal equilibrium with the radiation field; they are

Table 2. For the different cluster samples considered here: average redshifts (z), characteristic radii (θ_{500}) and total masses at a radius for which the mean cluster density is 500 and 200 times the critical density of the Universe ($M_{\rm tot}^{500}$ and $M_{\rm tot}^{200}$).

Sample	$\langle z \rangle$	$\langle \theta_{500} \rangle$ [arcmin]	$\langle M_{\rm tot}^{500} \rangle$ [$10^{14}\,M_\odot$]	$\langle M_{\rm tot}^{200} \rangle$ [$10^{14}\,M_\odot$]	β	$T_{\rm d0}$ [K] [K]	$M_{\rm dust}$ [$10^{10}\,M_\odot$]
Full sample	**0.26 ± 0.17**	**7.4 ± 5.3**	**5.1 ± 1.9**	**5.6 ± 2.1**	**1.5**	**19.2 ± 2.4**	**1.08 ± 0.32**
					2.2	15.3 ± 1.2	1.25 ± 0.36
					2.1	15.7 ± 1.2	1.24 ± 0.34
					2.0	16.2 ± 1.4	1.25 ± 0.37
					1.9	16.7 ± 1.5	1.24 ± 0.37
					1.8	17.2 ± 1.6	1.20 ± 0.35
					1.7	17.8 ± 1.8	1.17 ± 0.36
					1.6	18.5 ± 2.1	1.14 ± 0.34
					1.4	20.0 ± 2.8	1.03 ± 0.32
					1.3	20.9 ± 3.3	0.97 ± 0.32
$z \le 0.25$ (307)	0.139 ± 0.063	9.6 ± 6.3	4.0 ± 1.6	4.3 ± 1.7	1.5	20.7 ± 9.9	0.34 ± 0.17
$z > 0.25$ (254)	0.41 ± 0.13	4.68 ± 0.38	6.4 ± 1.3	7.0 ± 1.5	1.5	19.2 ± 3.2	2.56 ± 0.91
$M_{\rm tot}^{500} \le 5.5 \times 10^{14}\,M_\odot$ (320)	0.17 ± 0.11	9.1 ± 6.4	3.7 ± 1.1	4.1 ± 1.2	1.5	20.3 ± 5.1	0.21 ± 0.14
$M_{\rm tot}^{500} > 5.5 \times 10^{14}\,M_\odot$ (241)	0.38 ± 0.16	5.2 ± 1.7	6.8 ± 1.1	7.5 ± 1.2	1.5	19.2 ± 2.0	3.48 ± 0.99

Notes. The best-fit temperature and dust mass are also provided, exploring different choices for the emissivity index β for the full sample of 645 clusters.

stochastically heated and therefore their emission is not a simple modified blackbody (Compiègne et al. 2011; Jones et al. 2013). However, this additional contribution would be sub-dominant at $\lambda \ge 100\,\mu$m and so would not significantly change the derived temperature and mass of the cold dust, which corresponds to the bulk of the dust mass in galaxies (Cortese et al. 2012; Davies et al. 2012; Santini et al. 2014). We choose then to adopt a single-component approach and exclude the $60\,\mu$m from the data used for the fit. Not doing this would bias the estimate of the temperature and mass of the cold dust.

In Planck Collaboration Int. XXII (2015) the *Planck*-HFI intensity (and polarization) maps were used to estimate the spectral index β of the Galactic dust emission. On the basis of nominal mission data, they found that, at $\nu < 353$ GHz, the dust emission can be well represented by a modified blackbody spectrum with $\beta = 1.51 \pm 0.06$. At higher frequencies ($100\,\mu$m-353 GHz) $\beta = 1.65$ was assumed. In the following we have adopted a single spectral index over the whole spectral range, and $\beta = 1.5$ will be our baseline value. In some other studies an emissivity index $\beta = 2$ has been used instead, for example in the analysis of Davies et al. (2012), which focused on *Herschel* data (at $100-500\,\mu$m) to explore the IR properties of cluster galaxies (specifically 78 galaxies in the Virgo cluster).

4.2. Dust temperature and mass

By representing the recovered SEDs with a single-temperature modified blackbody dust model and fixing β, we can constrain the SED and estimate the average dust temperature. This is for the observer's frame, while the temperature in the rest-frame of the cluster will be given by $T_{\rm d} = T_{\rm d0}(1 + z)$.

We use a χ^2 minimization approach and account for colour corrections when comparing the measured SED to the modelled one. In Table 2 (upper line) we report the best-fit values that we obtain for $T_{\rm d0}$ and $M_{\rm dust}$[4] when considering the sample of 645 clusters, as well as the two redshift and mass sub-samples.

---

[4] We report $M_{\rm dust}$ rather than A_0, the overall amplitude to which it is proportional, see Sect. 4.2.

The associated uncertainties are derived from the statistical ones obtained through the χ^2 minimization in the fitting procedure (with $\Delta F_{\rm b}$ being the error on the flux at each frequency). The corresponding uncertainties on the dust mass estimates have been derived using random realizations of the model, letting $T_{\rm d0}$ and A_0 vary within the associated uncertainties and accounting for the correlation between the two. The best-fit models ($\beta = 1.5$) is represented in Figs. 4 by the black solid line. For the whole sample of 645 objects, we assume that the mean redshift is the mean of the known redshifts ($z = 0.26 \pm 0.17$). We then obtain $T_{\rm d} = (24.2 \pm 3.0 \pm 2.8)$ K, where the additional systematic uncertainty is due to the redshift dispersion of our sample (see the second column of Table 2), and an average dust mass of $(1.08 \pm 0.32) \times 10^{10}\,M_\odot$.

The recovered dust temperatures are in agreement with those observed for the dust content in various field galaxy samples (e.g. Dunne et al. 2011; Clemens et al. 2013; Symeonidis et al. 2013) and with the values expected for the cold dust component in cluster galaxies, e.g. the Virgo sample explored by Davies et al. (2012) and di Serego Alighieri et al. (2013). Our dust mass estimates are similar to those obtained with different approaches by Muller et al. (2008; $M_{\rm d} = 8 \times 10^9\,M_\odot$) for a sample with a comparable redshift distribution and Gutiérrez & López-Corredoira (2014; $M_{\rm d} < 8.4 \times 10^9\,M_\odot$) for a relatively low-mass cluster sample.

4.2.1. Additional sources of uncertainties and residual contamination

The spectral index β is known to vary with environment. Shown by *Planck* to be equal to 1.50 for the diffuse ISM in the Solar neighbourhood, β is known to be higher in molecular clouds (Planck Collaboration XI 2014). This reflects variations in the composition and structure of dust, something which is clearly seen in laboratory measurements (e.g. Jones et al. 2013). The impact of the adopted emissivity index on our results is explored by varying its value between 1.3 and 2.2. For the total sample of 645 clusters, we have explored how this affects $T_{\rm d0}$ and $M_{\rm dust}$, and we summarize the results in Table 2. When we compare the
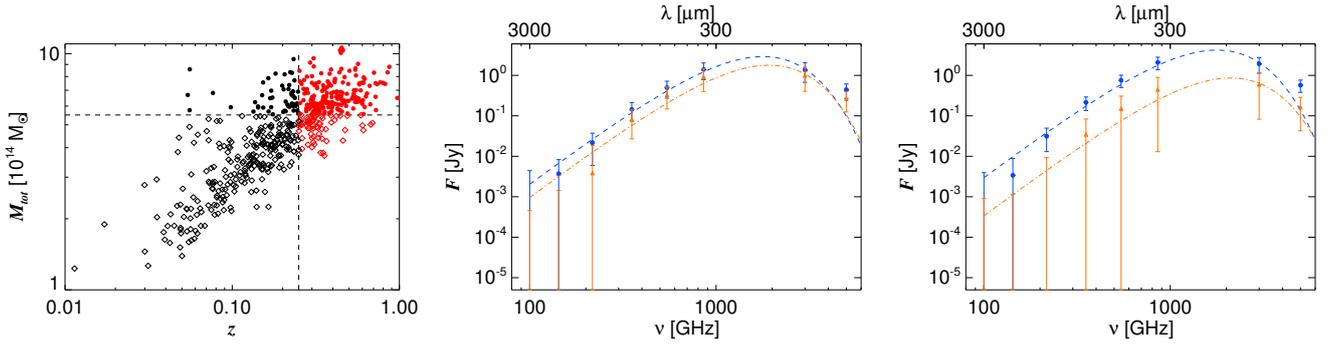
Fig. 5. SEDs for cluster sub-samples. *Left*: in the redshift−mass plane, we show the distribution of the 561 *Planck* clusters with known redshift, which are used in this paper. Different colours (black and red) are used for the low- and high-redshift sub-samples, while different symbols (dots and diamonds) are used for the low- and high-mass sub-samples. *Middle*: in blue circles the 254 clusters at $z > 0.25$ and in orange triangles the 307 clusters at $z \leq 0.25$ (307 clusters), plotted along with the corresponding best-fit models (dashed and dash-dotted lines, respectively). *Left*: in blue the 241 clusters with $M_{tot} > 5.5 \times 10^{14} M_\odot$ and in orange the 320 clusters with $M_{tot} \leq 5.5 \times 10^{14} M_\odot$, along with the best-fit models (dashed and dash-dotted lines, respectively). The rightmost (IRAS) point is not used in the fit.

dust temperature obtained with the same choice of β, i.e. $\beta = 2$, the dust temperatures that we find are similar to those obtained by Davies et al. (2012) for the galaxies of the Virgo cluster. The range explored shows that when reducing β the inferred T_0 increases, and vice versa, as expected given the degeneracy between these two parameters (e.g. Sajina et al. 2006; Désert et al. 2008; Kelly et al. 2012; Planck Collaboration Int. XIV 2014). However, the differences are not significant within the associated uncertainties, reflecting the fact that our data are not good enough to simultaneously constrain the temperature, the amplitude, and also the spectral index. Different values of β can affect the dust mass estimates by up to 20%, which is however negligible with respect to the existing uncertainty on the dust opacity κ_ν.

Figure 4 shows that the 143 and 353 GHz intensities are slightly lower and higher, respectively, with respect to the best-fit model. This might indicate a residual tSZ contamination, since the tSZ signal is negative at 143 GHz and positive at 353 GHz. The SZ amplitude that we subtract has been estimated under the non-relativistic hypothesis, and this could result in a slight underestimation of the cluster Comptonization parameter y. Although the relativistic correction is expected to have a small impact on the inferred Compton parameter, we should note that for cluster temperatures of a few Kelvin the relativistic correction boosts the tSZ flux at 857 by a factor of several tens of a percent. Given the amplitude of the SZ contribution at this frequency with respect to the dust emission, this contribution remains negligible. On the other hand, the cluster IR component we are considering here is not included in none of the simulations used to test the MILCA algorithm and might bias somehow the reconstruction of the tSZ amplitude. Then we have verified that the residual tSZ contamination is negligible by fitting, a posteriori, the dust SED as a linear combination of the modified blackbody and a tSZ contribution. For the two components we find an amplitude consistent with 1 and 0, respectively.

The normalization of the dust opacity represents the major source of uncertainty in deriving dust masses from observed IR fluxes (Fanciullo et al. 2015). The Draine (2003) value of κ_{850} was derived from a dust model (including assumptions about chemical composition, distribution of grain size, etc.) that shows good agreement with available data. However, using a different approach, James et al. (2002) found $\kappa_{850} = (0.07 \pm 0.02) \, \mathrm{m^2 \, kg^{-1}}$, nearly a factor of 2 higher. The latter value uses a calibration that has been obtained with a sample of galaxies for which the IR fluxes, gas masses, and metallicities are all

available, and adopts the assumption that the fraction of metals bound up in dust is constant for all the galaxies in the sample. Planck Collaboration Int. XXIX (2016) has shown that the opacity of the Draine (2003) model needs to be increased by a factor of 1.8 to fit the *Planck* data, as well as extinction measurements, and this moves the normalization towards the value suggested by James et al. (2002).

4.2.2. Possible evolution with mass and redshift

As a first attempt to investigate how clusters of different mass and at different redshift contribute to the overall average signal, we have divided our sample into two different sub-samples, according to their redshifts and their masses. An increased IR emission with redshift was in fact seen in Planck Collaboration XXIII (2016; for $z < 0.15$ versus $z > 0.15$), in which a similar stacking was performed on *Planck* data to investigate the cross-correlation between the tSZ effect and the CIB fluctuations. This is expected since in more distant (younger) clusters there will be more gas-rich active (i.e. star-forming) spirals. Conversely, nearby clusters mainly contain elliptical galaxies, with a lower star-formation rate and little dust. But we also expect the overall IR signal to be higher for higher mass objects. We expect dust emission to be proportional to the total cluster mass because they should both be tightly correlated with the number of galaxies (Giard et al. 2008; da Silva et al. 2009).

We have considered clusters above and below $z = 0.25$ (with 254 and 307 sources, respectively) and above and below $M_{tot}^{500} = 5.5 \times 10^{14} M_\odot$ (241 and 320 sources, respectively)[5]. The left panel in Fig. 5 provides the $z - M_{tot}$ distribution of the 561 *Planck* clusters with known redshift used in this paper. This figure shows that the two partitions do not trace exactly the same populations, but they are also not completely independent. The lower redshift bin strongly overlaps with lower mass systems and vice versa. The middle and right panels show the measured SED for the low (orange) and high (blue) redshift and mass sub-samples, respectively.

For the low-redshift and low-mass sub-samples we have no detection at $\nu < 353$ GHz (Fig. 5, middle panel). The SEDs for the two redshift sub-samples are consistent with each other (within ΔF_b), even though fluxes are systematically higher at

---

[5] M_{tot}^{500} is the total mass contained within a radius (θ_{500}) at which the mean cluster density is 500 times the critical density of the Universe.

higher z. For the high- and low-mass sub-samples, the difference between the two SEDs becomes more important, with higher fluxes when $M_{tot}^{500} > 5.5 \times 10^{14} \, M_\odot$ (Fig. 5, right panel). A similar behaviour for the sub-samples in M_{tot}^{500} and z is not surprising, given the correlation between the two (Fig. 5, left panel).

In Table 2 we list the best fit parameters obtained for the four sub-samples. We observe a slight increase of dust temperature with mass and redshift, but no significant evolution within the uncertainties. On the other side, for the low- and high-mass sub-samples we find significantly different values of the overall dust mass, implying that the dust mass is responsible for the difference between the two curves in the middle panel of Fig. 5 and that the evolution we observe, also in z, is manly due to the correlation between M_d and M_{tot}.

4.3. Dust-to-gas mass ratio

We now estimate the ratio of dust mass to gas mass, Z_d, directly from the observed IR cluster signal. To do so we need an estimate of the cluster gas mass. The IR fluxes used in the previous section to estimate M_d were obtained by integrating the signal out to 15′ from the cluster centres, without any rescaling of the maps with respect to each cluster's characteristic radius. In the PSZ1, the mass information is provided at θ_{500}, and for our sample this size is significantly smaller than 15′ for almost all clusters (see Table 2). However, we can take advantage of the self-similarity of cluster profiles, from which it follows that the ratio between radii corresponding to different overdensities is nearly constant over the cluster population. Therefore we will use θ_{200} and assume that $\theta_{200} \simeq 1.4 \times \theta_{500}$ (Ettori & Balestra 2009) to obtain the corresponding enclosed total mass $M_{tot}^{200} = (4\pi\rho_c\theta_{200}^3)/3$. Here, θ_{500} is obtained from the M_{tot}^{500} values listed in the PSZ1. The cluster total mass also provides an estimate of the gas mass, $M_{gas}^{200} \simeq 0.1 \, M_{tot}^{200}$ (e.g. Pratt et al. 2009; Comis et al. 2011; Planck Collaboration Int. V 2013; Sembolini et al. 2013). Assuming that M_d and M_{tot}^{200} correspond to comparable cluster regions, we find that $Z_d = (1.93 \pm 0.92) \times 10^{-4}$ for the full sample. For the low- and high-redshift sub-samples we find $(0.79 \pm 0.50) \times 10^{-4}$ and $(3.7 \pm 1.5) \times 10^{-4}$, respectively, while for the low- and high-mass sub-samples we obtain $(0.51 \pm 0.37) \times 10^{-4}$ and $(4.6 \pm 1.5) \times 10^{-4}$, respectively. We note that the uncertainties quoted here do not account for the fact that the gas fraction might vary from cluster to cluster, and as a function of radius/mass and redshift.

These dust-to-mass ratios are derived from the overall IR flux, which is the sum of the contribution due to the cluster galaxies and a possible further contribution coming from the ICM dust component. Therefore they represent an upper limit for the dust fraction that is contained within the IGM/ICM. These values are consistent with the upper limit (5×10^{-4}) derived by Giard et al. (2008) from the L_{IR}/L_X ratio and a model for the ICM dust emission (Montier & Giard 2004).

5. Conclusions

We have adopted a stacking approach in order to recover for the first time, the average SED of the IR emission towards galaxy clusters. Considering the Catalogue of *Planck* SZ Clusters, we have used the *Planck*-HFI maps (from 100 to 857 GHz) and the IRAS maps (IRIS data at 100 and 60 μm) in order to sample the SED of the cluster dust emission on both sides of the expected emissivity peak.

For a sample of 645 clusters selected from the PSZ1 catalogue, we find significant detection of dust emission from 353 to 857 GHz, and at 100 μm and 60 μm, at the cluster positions, after cleaning for foreground contributions. By co-adding maps extracted at random positions on the sky, we have verified that the residual Galactic emission is accounted for in the uncertainty budget. For the IRAS frequencies, we find average central intensities that are in agreement with the values found by Montier & Giard (2005). The measured SED is consistent with dust IR emission following a modified blackbody distribution.

These results have allowed us to constrain, directly from its IR emission, both the average overall dust temperature and the dust mass in clusters. From the average cluster SED of a total sample of 645 clusters, we infer an average dust temperature of $T_d = (24.2 \pm 3.0) \, K$, in agreement with what is observed for galaxy thermal dust emission and an average dust mass of $M_d = (1.25 \pm 0.37) \times 10^{10} \, M_\odot$. By dividing our initial sample into two bins, according to either their mass or redshift, we find that the IR emission is larger for the higher mass (or higher redshift) clusters. This difference is mainly due to the positive correlation between dust mass and cluster total mass, the resulting IR emission being proportional to the latter. Our sample is not ideal for taking the next step and constraining the mass and redshift evolution of the IR emission of the cluster dust component because it is not complete and we do not dispose of a well-characterized selection function for it. Furthermore, the redshift and mass bins, although they do not trace exactly the same cluster population, are not independent either. With a larger sample, and a wider distribution in mass and redshift, the separate mass and redshift dependance could be studied much more thoroughly, for example by correlating the weak signals from individual clusters with M_{tot} and z. This approach would allow us to better account for different distances, masses, and selection effects.

Using the total mass estimates for each cluster, we also derive the average cluster dust-to-gas mass ratio $Z_d = (1.93 \pm 0.92) \times 10^{-4}$. This leads to an upper limit on the dust fraction within the ICM that is consistent with previous results. Most of the IR signal detected in the maps stacked at cluster positions was expected to be due to the contribution of the member galaxies (e.g. Roncarelli et al. 2010). And the recovered temperature, typical of values found in the discs of galaxies, is in agreement with this. However, if we also take into account the additional uncertainties on the dust mass estimates coming from the spectral index and the dust opacity (up to 20% and 50%, respectively), our results cannot exclude a dust fraction that, according to Montier & Giard 2004, would imply that the IR ICM dust emission is an important factor in the cooling of the intra-cluster gas.

References

Bavouzet, N., Dole, H., Le Floc'h, E., et al. 2008, A&A, 479, 83
Béthermin, M., Dole, H., Beelen, A., & Aussel, H. 2010, A&A, 512, A78

Braglia, F. G., Ade, P. A. R., Bock, J. J., et al. 2011, MNRAS, 412, 1187
Casey, C. M. 2012, MNRAS, 425, 3094
Chelouche, D., Koester, B. P., & Bowen, D. V. 2007, ApJ, 671, L97
Clemens, M. S., Negrello, M., De Zotti, G., et al. 2013, MNRAS, 433, 695
Comis, B., de Petris, M., Conte, A., Lamagna, L., & de Gregori, S. 2011, MNRAS, 418, 1089
Compiègne, M., Verstraete, L., Jones, A., et al. 2011, A&A, 525, A103
Coppin, K. E. K., Geach, J. E., Smail, I., et al. 2011, MNRAS, 416, 680
Cortese, L., Ciesla, L., Boselli, A., et al. 2012, A&A, 540, A52
da Silva, A. C., Catalano, A., Montier, L., et al. 2009, MNRAS, 396, 849
Dale, D. A., & Helou, G. 2002, ApJ, 576, 159
Davies, J. I., Bianchi, S., Cortese, L., et al. 2012, MNRAS, 419, 3505
Désert, F.-X., Macías-Pérez, J. F., Mayet, F., et al. 2008, A&A, 481, 411
di Serego Alighieri, S., Bianchi, S., Pappalardo, C., et al. 2013, A&A, 552, A8
Draine, B. T. 2003, ARA&A, 41, 241
Draine, B. T., & Li, A. 2007, ApJ, 657, 810
Dunne, L., Gomez, H. L., da Cunha, E., et al. 2011, MNRAS, 417, 1510
Dwek, E., & Arendt, R. G. 1992, ARA&A, 30, 11
Dwek, E., Rephaeli, Y., & Mather, J. C. 1990, ApJ, 350, 104
Ettori, S., & Balestra, I. 2009, A&A, 496, 343
Fanciullo, L., Guillet, V., Aniano, G., et al. 2015, A&A, 580, A136
Giard, M., Montier, L., Pointecouteau, E., & Simmat, E. 2008, A&A, 490, 547
Gorski, K. M., Wandelt, B. D., Hansen, F. K., Hivon, E., & Banday, A. J. 1999, ArXiv e-print [arXiv:astro-ph/9905275]
Górski, K. M., Hivon, E., Banday, A. J., et al. 2005, ApJ, 622, 759
Gutiérrez, C. M., & López-Corredoira, M. 2014, A&A, 571, A66
Helou, G., & Walker, D. W. 1988, Infrared astronomical satellite (IRAS) catalogs and atlases, Volume 7: The small scale structure catalog
Hildebrand, R. H. 1983, Quant. J. Rev. Astron. Soc., 24, 267
Hurier, G., Macías-Pérez, J. F., & Hildebrandt, S. 2013, A&A, 558, A118
James, A., Dunne, L., Eales, S., & Edmunds, M. G. 2002, MNRAS, 335, 753
Jones, A. P., Fanciullo, L., Köhler, M., et al. 2013, A&A, 558, A62
Kelly, D. M., & Rieke, G. H. 1990, ApJ, 361, 354
Kelly, B. C., Shetty, R., Stutz, A. M., et al. 2012, ApJ, 752, 55
Kitayama, T., Ito, Y., Okada, Y., et al. 2009, ApJ, 695, 1191
Miville-Deschênes, M.-A., & Lagache, G. 2005, ApJS, 157, 302
Montier, L. A., & Giard, M. 2004, A&A, 417, 401
Montier, L. A., & Giard, M. 2005, A&A, 439, 35
Muller, S., Wu, S.-Y., Hsieh, B.-C., et al. 2008, ApJ, 680, 975
Planck Collaboration IX. 2014, A&A, 571, A9
Planck Collaboration XI. 2014, A&A, 571, A11
Planck Collaboration, Ade, P. A. R., Aghanim, N., et al. 2014, A&A, 571, A13
Planck Collaboration XXI. 2014, A&A, 571, A21
Planck Collaboration XXIX. 2014, A&A, 571, A29
Planck Collaboration XXXII 2015, A&A, 581, A14
Planck Collaboration I. 2016, A&A, 594, A1
Planck Collaboration XXII. 2016, A&A, 594, A22
Planck Collaboration XXIII. 2016, A&A, 594, A23
Planck Collaboration XXVII. 2016, A&A, 594, A27
Planck Collaboration Int. V. 2013, A&A, 550, A131
Planck Collaboration Int. XIV. 2014, A&A, 564, A45
Planck Collaboration Int. XXII. 2015, A&A, 576, A107
Planck Collaboration Int. XXVI. 2015, A&A, 582, A29
Planck Collaboration Int. XXIX. 2016, A&A, 586, A132
Planck Collaboration Int. XXXVI. 2016, A&A, 586, A139
Popescu, C. C., Tuffs, R. J., Fischera, J., & Völk, H. 2000, A&A, 354, 480
Pratt, G. W., Croston, J. H., Arnaud, M., & Böhringer, H. 2009, A&A, 498, 361
Roncarelli, M., Pointecouteau, E., Giard, M., Montier, L., & Pello, R. 2010, A&A, 512, A20
Sajina, A., Scott, D., Dennefeld, M., et al. 2006, MNRAS, 369, 939
Santini, P., Maiolino, R., Magnelli, B., et al. 2014, A&A, 562, A30
Sarazin, C. L. 1986, Rev. Mod. Phys., 58, 1
Sarazin, C. L. 1988, X-ray emission from clusters of galaxies (Campridge University Press)
Sembolini, F., Yepes, G., De Petris, M., et al. 2013, MNRAS, 429, 323
Stickel, M., Klaas, U., Lemke, D., & Mattila, K. 2002, A&A, 383, 367
Sunyaev, R. A., & Zeldovich, Y. B. 1972, Comm. Astrophys. Space Phys., 4, 173
Sunyaev, R. A., & Zeldovich, I. B. 1980, ARA&A, 18, 537
Symeonidis, M., Vaccari, M., Berta, S., et al. 2013, MNRAS, 431, 2317
Weingartner, J. C., Draine, B. T., & Barr, D. K. 2006, ApJ, 645, 1188
Welikala, N., Béthermin, M., Guery, D., et al. 2016, MNRAS, 455, 1629
Wiklind, T. 2003, ApJ, 588, 736

Cité, 10 rue Alice Domon et Léonie Duquet, 75205 Paris Cedex 13, France

[2] Aalto University Metsähovi Radio Observatory and Dept of Radio Science and Engineering, PO Box 13000, 00076 Aalto, Finland

[3] Academy of Sciences of Tatarstan, Bauman Str., 20, 420111 Kazan, Republic of Tatarstan, Russia

[4] African Institute for Mathematical Sciences, 6−8 Melrose Road, Muizenberg, 7945 Cape Town, South Africa

[5] Agenzia Spaziale Italiana Science Data Center, via del Politecnico snc, 00133 Roma, Italy

[6] Aix Marseille Université, CNRS, LAM (Laboratoire d'Astrophysique de Marseille) UMR 7326, 13388 Marseille, France

[7] Astrophysics Group, Cavendish Laboratory, University of Cambridge, J J Thomson Avenue, Cambridge CB3 0HE, UK

[8] Astrophysics & Cosmology Research Unit, School of Mathematics, Statistics & Computer Science, University of KwaZulu-Natal, Westville Campus, Private Bag X54001, 4000 Durban, South Africa

[9] Atacama Large Millimeter/submillimeter Array, ALMA Santiago Central Offices, Alonso de Cordova 3107, Vitacura, Casilla 763 0355 Santiago, Chile

[10] CGEE, SCS Qd 9, Lote C, Torre C, 4° andar, Ed. Parque Cidade Corporate, CEP 70308-200, Brasília, DF, Brazil

[11] CITA, University of Toronto, 60 St. George St., Toronto, ON M5S 3H8, Canada

[12] CNRS, IRAP, 9 Av. colonel Roche, BP 44346, 31028 Toulouse Cedex 4, France

[13] California Institute of Technology, Pasadena, California, USA

[14] Centro de Estudios de Física del Cosmos de Aragón (CEFCA), Plaza San Juan, 1, planta 2, 44001 Teruel, Spain

[15] Computational Cosmology Center, Lawrence Berkeley National Laboratory, Berkeley, California, CA 94720, USA

[16] Consejo Superior de Investigaciones Científicas (CSIC), 28049 Madrid, Spain

[17] DSM/Irfu/SPP, CEA-Saclay, 91191 Gif-sur-Yvette Cedex, France

[18] DTU Space, National Space Institute, Technical University of Denmark, Elektrovej 327, 2800 Kgs. Lyngby, Denmark

[19] Département de Physique Théorique, Université de Genève, 24, Quai E. Ansermet, 1211 Genève 4, Switzerland

[20] Departamento de Astrofísica, Universidad de La Laguna (ULL), 38206 La Laguna, Tenerife, Spain

[21] Departamento de Física, Universidad de Oviedo, Avda. Calvo Sotelo s/n, 33077 Oviedo, Spain

[22] Department of Astronomy and Geodesy, Kazan Federal University, Kremlevskaya Str., 18, 420008 Kazan, Russia

[23] Department of Astrophysics/IMAPP, Radboud University Nijmegen, PO Box 9010, 6500 GL Nijmegen, The Netherlands

[24] Department of Physics & Astronomy, University of British Columbia, 6224 Agricultural Road, Vancouver, British Columbia, Canada

[25] Department of Physics and Astronomy, Dana and David Dornsife College of Letter, Arts and Sciences, University of Southern California, Los Angeles, CA 90089, USA

[26] Department of Physics and Astronomy, University College London, London WC1E 6BT, UK

[27] Department of Physics, Gustaf Hällströmin katu 2a, University of Helsinki, 00100 Helsinki, Finland

[28] Department of Physics, Princeton University, Princeton, New Jersey, NJ 08544, USA

[29] Department of Physics, University of California, Santa Barbara, California, CA 93106 USA

[30] Dipartimento di Fisica e Astronomia G. Galilei, Università degli Studi di Padova, via Marzolo 8, 35131 Padova, Italy

[31] Dipartimento di Fisica e Scienze della Terra, Università di Ferrara, via Saragat 1, 44122 Ferrara, Italy

[32] Dipartimento di Fisica, Università La Sapienza, P. le A. Moro 2, 00133 Roma, Italy

[33] Dipartimento di Fisica, Università degli Studi di Milano, via Celoria 16, 20133 Milano, Italy

[1] APC, AstroParticule et Cosmologie, Université Paris Diderot, CNRS/IN2P3, CEA/lrfu, Observatoire de Paris, Sorbonne Paris

[34] Dipartimento di Fisica, Università degli Studi di Trieste, via A. Valerio 2, 34127 Trieste, Italy

[35] Dipartimento di Matematica, Università di Roma Tor Vergata, via della Ricerca Scientifica, 1, 00133 Roma, Italy

[36] Discovery Center, Niels Bohr Institute, Blegdamsvej 17, 1165 Copenhagen, Denmark

[37] Discovery Center, Niels Bohr Institute, Copenhagen University, Blegdamsvej 17, 1165 Copenhagen, Denmark

[38] European Southern Observatory, ESO Vitacura, Alonso de Cordova 3107, Vitacura, Casilla 19001 Santiago, Chile

[39] European Space Agency, ESAC, Planck Science Office, Camino bajo del Castillo, s/n, Urbanización Villafranca del Castillo, Villanueva de la Cañada, Madrid, Spain

[40] European Space Agency, ESTEC, Keplerlaan 1, 2201 AZ Noordwijk, The Netherlands

[41] Gran Sasso Science Institute, INFN, viale F. Crispi 7, 67100 L'Aquila, Italy

[42] HGSFP and University of Heidelberg, Theoretical Physics Department, Philosophenweg 16, 69120 Heidelberg, Germany

[43] Helsinki Institute of Physics, Gustaf Hällströmin katu 2, University of Helsinki, 35131 Helsinki, Finland

[44] INAF−Osservatorio Astronomico di Padova, Vicolo dell'Osservatorio 5, 35131 Padova, Italy

[45] INAF−Osservatorio Astronomico di Roma, via di Frascati 33, Monte Porzio Catone, Italy

[46] INAF−Osservatorio Astronomico di Trieste, via G.B. Tiepolo 11, Trieste, Italy

[47] INAF/IASF Bologna, via Gobetti 101, Bologna, Italy

[48] INAF/IASF Milano, via E. Bassini 15, Milano, Italy

[49] INFN, Sezione di Bologna, viale Berti Pichat 6/2, 40127 Bologna, Italy

[50] INFN, Sezione di Ferrara, via Saragat 1, 44122 Ferrara, Italy

[51] INFN, Sezione di Roma 1, Università di Roma Sapienza, Piazzale Aldo Moro 2, 00185 Roma, Italy

[52] INFN, Sezione di Roma 2, Università di Roma Tor Vergata, via della Ricerca Scientifica, 1, 00185 Roma, Italy

[53] INFN/National Institute for Nuclear Physics, via Valerio 2, 34127 Trieste, Italy

[54] IPAG: Institut de Planétologie et d'Astrophysique de Grenoble, Université Grenoble Alpes, IPAG, CNRS, IPAG, 38000 Grenoble, France

[55] Imperial College London, Astrophysics group, Blackett Laboratory, Prince Consort Road, London, SW7 2AZ, UK

[56] Infrared Processing and Analysis Center, California Institute of Technology, Pasadena, CA 91125, USA

[57] Institut Universitaire de France, 103 bd Saint-Michel, 75005 Paris, France

[58] Institut d'Astrophysique Spatiale, CNRS, Univ. Paris-Sud, Université Paris-Saclay, Bât. 121, 91405 Orsay Cedex, France

[59] Institut d'Astrophysique de Paris, CNRS (UMR7095), 98bis Boulevard Arago, 75014 Paris, France

[60] Institute of Astronomy, University of Cambridge, Madingley Road, Cambridge CB3 0HA, UK

[61] Institute of Theoretical Astrophysics, University of Oslo, Blindern, 38106 Oslo, Norway

[62] Instituto de Astrofísica de Canarias, C/Vía Láctea s/n, La Laguna, 38205 Tenerife, Spain

[63] Instituto de Física de Cantabria (CSIC-Universidad de Cantabria), Avda. de los Castros s/n, 39005 Santander, Spain

[64] Istituto Nazionale di Fisica Nucleare, Sezione di Padova, via Marzolo 8, 35131 Padova, Italy

[65] Jet Propulsion Laboratory, California Institute of Technology, 4800 Oak Grove Drive, Pasadena, California, USA

[66] Jodrell Bank Centre for Astrophysics, Alan Turing Building, School of Physics and Astronomy, The University of Manchester, Oxford Road, Manchester, M13 9PL, UK

[67] Kavli Institute for Cosmology Cambridge, Madingley Road, Cambridge, CB3 0HA, UK

[68] Kazan Federal University, 18 Kremlyovskaya St., 420008 Kazan, Russia

[69] LAL, Université Paris-Sud, CNRS/IN2P3, Orsay, France

[70] LERMA, CNRS, Observatoire de Paris, 61 Avenue de l'Observatoire, 75000 Paris, France

[71] Laboratoire AIM, IRFU/Service d'Astrophysique − CEA/DSM − CNRS − Université Paris Diderot, Bât. 709, CEA-Saclay, 91191 Gif-sur-Yvette Cedex, France

[72] Laboratoire Traitement et Communication de l'Information, CNRS (UMR 5141) and Télécom ParisTech, 46 rue Barrault, 75634 Paris Cedex 13, France

[73] Laboratoire de Physique Subatomique et Cosmologie, Université Grenoble-Alpes, CNRS/IN2P3, 53 rue des Martyrs, 38026 Grenoble Cedex, France

[74] Laboratoire de Physique Théorique, Université Paris-Sud 11 & CNRS, Bâtiment 210, 91405 Orsay, France

[75] Lawrence Berkeley National Laboratory, Berkeley, CA 94720 California, USA

[76] Lebedev Physical Institute of the Russian Academy of Sciences, Astro Space Centre, 84/32 Profsoyuznaya st., 117997 Moscow, GSP-7, Russia

[77] Max-Planck-Institut für Astrophysik, Karl-Schwarzschild-Str. 1, 85741 Garching, Germany

[78] Moscow Institute of Physics and Technology, Dolgoprudny, Institutsky per., 9, 141700 Moscow, Russia

[79] National University of Ireland, Department of Experimental Physics, Maynooth, Co. Kildare, Ireland

[80] Nicolaus Copernicus Astronomical Center, Bartycka 18, 00-716 Warsaw, Poland

[81] Niels Bohr Institute, Blegdamsvej 17, 1165 Copenhagen, Denmark

[82] Niels Bohr Institute, Copenhagen University, Blegdamsvej 17, Copenhagen, Denmark

[83] Nordita (Nordic Institute for Theoretical Physics), Roslagstullsbacken 23, 106 91 Stockholm, Sweden

[84] Optical Science Laboratory, University College London, Gower Street, WC1E6BT London, UK

[85] SISSA, Astrophysics Sector, via Bonomea 265, 34136 Trieste, Italy

[86] SMARTEST Research Centre, Università degli Studi e-Campus, via Isimbardi 10, 22060 Novedrate (CO), Italy

[87] School of Physics and Astronomy, Cardiff University, Queens Buildings, The Parade, Cardiff, CF24 3AA, UK

[88] Sorbonne Université-UPMC, UMR7095, Institut d'Astrophysique de Paris, 98bis Boulevard Arago, 75014 Paris, France

[89] Space Research Institute (IKI), Russian Academy of Sciences, Profsoyuznaya Str, 84/32, 117997 Moscow, Russia

[90] Space Sciences Laboratory, University of California, Berkeley, California, CA 94720 USA

[91] Special Astrophysical Observatory, Russian Academy of Sciences, Nizhnij Arkhyz, Zelenchukskiy region, 369167 Karachai-Cherkessian Republic, Russia

[92] Sub-Department of Astrophysics, University of Oxford, Keble Road, Oxford OX1 3RH, UK

[93] TÜBİTAK National Observatory, Akdeniz University Campus, 07058 Antalya, Turkey

[94] The Oskar Klein Centre for Cosmoparticle Physics, Department of Physics,Stockholm University, AlbaNova, 106 91 Stockholm, Sweden

[95] UPMC Univ Paris 06, UMR7095, 98bis Boulevard Arago, 75014 Paris, France

[96] Université de Toulouse, UPS-OMP, IRAP, 31028 Toulouse Cedex 4, France

[97] University of Granada, Departamento de Física Teórica y del Cosmos, Facultad de Ciencias, 18071 Granada, Spain

[98] University of Granada, Instituto Carlos I de Física Teórica y Computacional, 18071 Granada, Spain

[99] Warsaw University Observatory, Aleje Ujazdowskie 4, 00-478 Warszawa, Poland
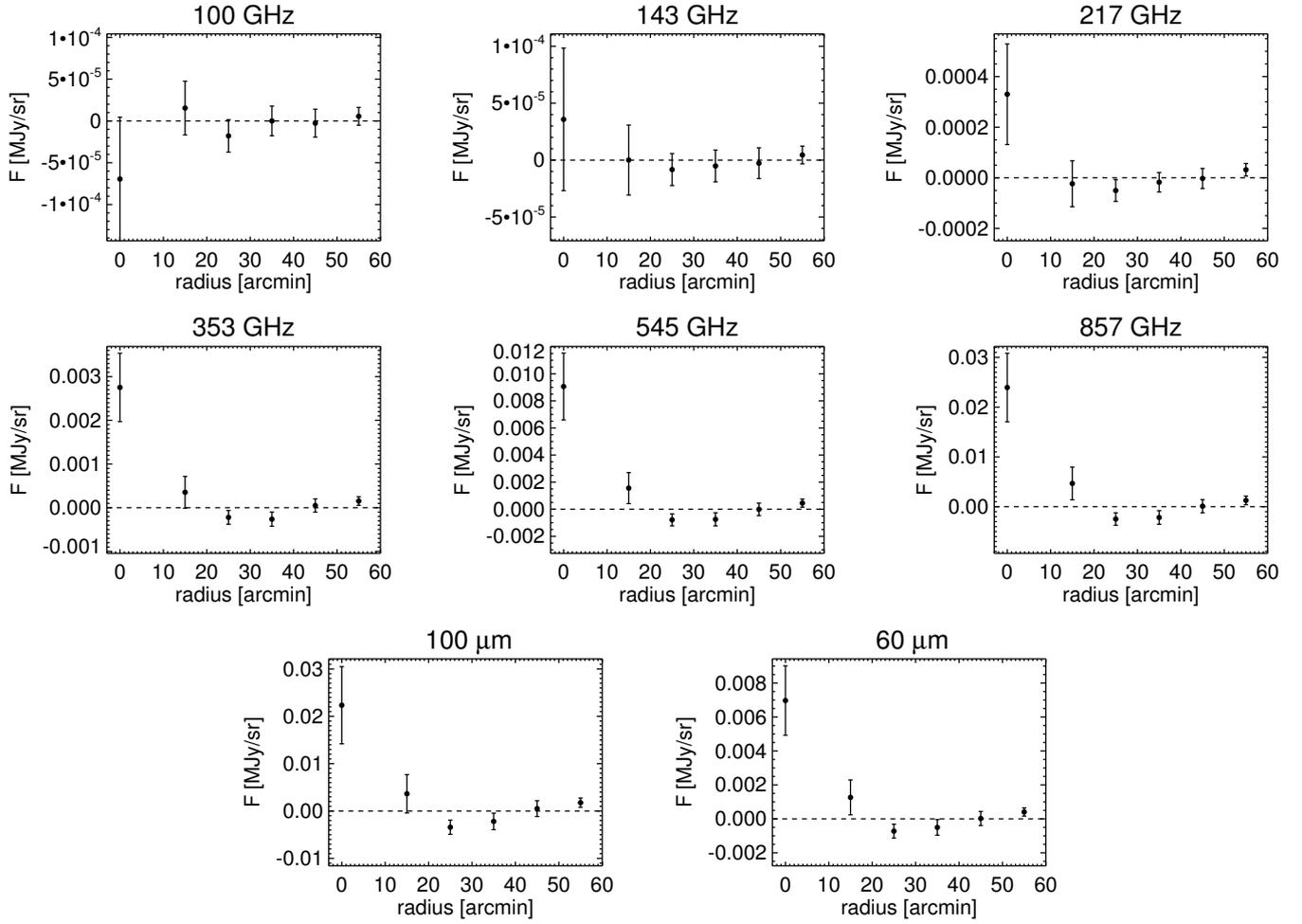
Appendix A: Additional figure

Fig. A.1. Radial profiles obtained from the background- and foreground-cleaned stacked maps, for the sample of 645 clusters. The units here are MJy sr^{-1}. The black points correspond to the values obtained as the average of the pixels contained within each region considered and associated uncertainties have been obtained using bootstrap resampling. We find no significant detection at 100 and 143 GHz, while the detection starts to become strong at $\nu \geq 353$ GHz, consistent with what we saw in Fig. 2.